This paper is published in Langmuir 36, 17, 4835—4841 (2020)
https://doi.org/10.1021/acs.langmuir.0c00193

Making photonic crystals via evaporation of nanoparticle-laden droplets on superhydrophobic microstructures[†]

Masoud Bozorg Bigdeli and Peichun Amy Tsai*

Department of Mechanical Engineering, University of Alberta, Edmonton, Alberta T6G 2G8, Canada

E-mail: peichun.amy.tsai@ualberta.ca

Abstract

We employed a convenient evaporation approach to fabricate photonic crystals by naturally drying droplets laden with nanoparticles on a superhydrophobic surface. The final drying morphology could be controlled by the concentration of nanoparticles. A dilute droplet resulted in a torus, whereas a quasi-spherical cap with a bottom cavity was made from a concentrated droplet. Remarkably, the nanofluid droplets maintained high contact angles ($\gtrsim 120°$) during the entire evaporation process due to inhomogeneous surface wetting. Bottom-view snapshots revealed that during evaporation the color of the contact area changed sequentially from white to red, orange, yellow and eventually to green. Scanning electron microscopy and Voronoi analysis demonstrated that nanoparticles were self-assembled to a hexagonal pattern. Finally, based on the effects of particle size, material, and volume concentration on the reflected wavelengths, a model has been developed to successfully predict the reflected wavelength peaks from the contact area of evaporating colloidal droplets. Our model can be easily adopted as a manufacture guide of functional photonic crystals to predict the optimal reflected color made by evaporation-driven self-assembly of photonic crystals.

Introduction

A significant step toward effective use of nanomaterials in a variety of applications, such as flexible electronics,[1] optical,[2] thermal[3,4] and nanofluidic devices,[5] is the fabrication of robust nanostructures. Photonic crystals (PhCs), in particular, have attracted a great deal of attention due to their ability to control and guide photons in a manner analogous to the capability of electronic crystals to manipulate electrons. The ability to control photons makes PhCs ideal candidates for a range of applications, including a colorimetric detection of protein,[6] catalyst supports,[7] as well as thermal, magnetic, electrical, mechanical, chemical and optical sensing.[8,9] Photonic crystals can be manufactured using top-down and bottom-up methods in two (2D) and three (3D) dimensions.[10–12] Top-down approaches consist of lithography with ions, atoms, electrons, and photons. Bottom-up techniques consist of particle assembly driven by gravitational,[13] electric[14] and magnetic fields,[15] as well as assembly through (solvent) evaporation.[16]

Bottom-up assembly techniques are increasingly preferred, on account of the ease of process, the lower cost, and the production potential at an industrial scale.[17] Among bottom-up methods, using the evaporative self-assembly mechanism is a well established technique for the fabrication of 2D photonic crystals.

[†] Supplementary Material is available online.

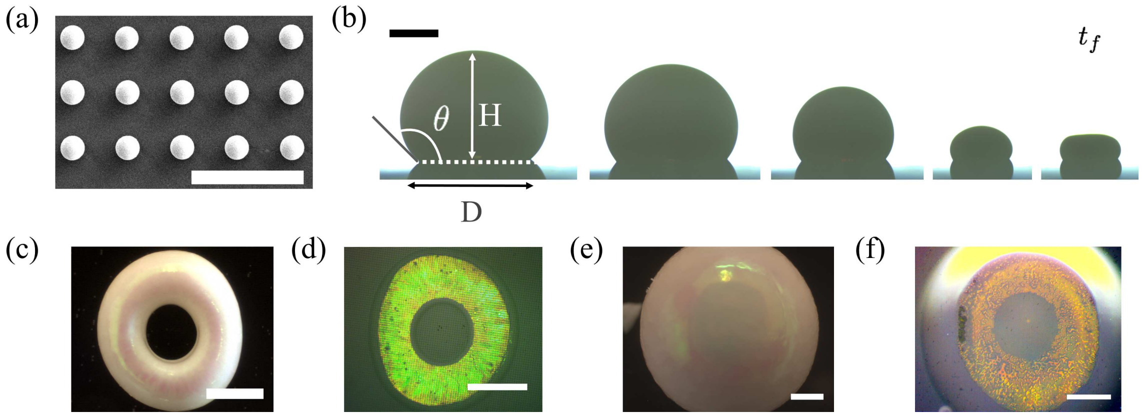

Figure 1: (a) Scanning electron microscopy (SEM) image of the top-view superhydrophobic surface used. Scale bar corresponds to 30 μm. (b) Side-view snapshots of an evaporating droplet containing 5 wt% silica nanoparticles on superhydrophobic substrate. The scale bar in (b) corresponds to 1 mm, and the time-scale of complete drying, $t_f = 4770$ s. Optical microscope images of fabricated photonic crystals in (c) to (f). (c) top-view and (d) bottom-view images of the toroidal deposit pattern corresponding to water droplets laden with low concentration (≈ 5 wt%) of NPs. (e) top-view and (f) bottom-view images of the spherical deposit pattern resulting from evaporation of high concentration (60 ± 5 $wt\%$) colloidal drops. The vivid color in (d) and (f), observed close to a complete dry time (at t_f and $0.97t_f$, respectively), is the reflectance color scattered by the bottom of the resultant self-assembly of photonic crystals. Scale bars in (c) to (f) are 500 μm.

However, the complex nature of the self-assembly methods introduced for creating 3D photonic crystals, including acoustic levitation,[18] inkjet printing[19] and emulsion solvent evaporation,[20,21] suggests that there is room for further development.

Superhydrophobic (SH) surfaces have been intensively studied in recent decades, owing to their non-sticking and self-cleaning properties.[22–24] Primarily researchers have been interested in their fabrication as well as the wetting states and transition of water droplets on superhydropohobic surfaces of varying geometric features.[22,25–34] Relatively few studies (albeit with an increasing number) have focused on 3D depositions of various materials through evaporative self-assembly on superhydrophobic surfaces. Some examples include drying droplets of protein (lysozyme) solution,[35] suspensions of micro-particles,[36,37] colloidal semiconductor (CdSe/CdS) nanorods,[38] colloidal polymer dispersion,[39] and suspension of Latex nanoparticles (NPs),[40] ceramic (alumina) NPs[41] or multi-component colloidal dispersion droplets,[42,43] on superhydrophobic surfaces. In particular, compact and ball-liked structural packing has been synthesized by drying dilute “Fakir" (or Cassie-Baxter heterogeneous wetting[44]) suspensions of microparticles without a pinned contact line on superhydrophobic surfaces.[36,45] In addition, the packing structure and elastic modulus of the resultant “supraball” can be tuned by using pH-responsive microparticles via a pH change. The suspension with pH=3 led to a spherical-shaped particle assembly of high ordering, whereas with pH=10 an oblate-shaped and disordered assembly with a lower packing fraction.[46] However, systematic investigations of contact angle evolution, different wetting states, and transient photonic color sequences concerning the evaporation of NP-colloidal droplets on superhydrophobic surfaces, with the intention of making light diffracting 3D photonic crystals, are still rare.

In this paper, we have exploited the effect of particle concentration and have chosen a proper superhydrophobic substrate for the facile creation of 3D photonic crystals. Specifically, colloidal drops with two distinct initial concentrations were left on a superhydrophobic surface to evaporate at ambient conditions. Through this simplistic and reproducible technique we were able to fabricate structural photonic crystals with two different morphologies: donut-shaped (toroidal) and quasi-spherical for the low and high particle concentrations, respectively. Furthermore, we have investigated the evaporation dynamics, the packing, and the reflection peaks of these self-assembled nanoparticles forming photonic crystals.

Experimental

The superhydrophobic substrates were fabricated through a replica molding process using Polydimethylsiloxane (PDMS) .[33,47–51] Substrates were transparent and consisted of parallel cylindrical pillars forming a square pattern of an area size about 2×2 cm^2. The scanning electron microscope (SEM) image of the superhydrophobic surface texture is shown in Fig. 1a. The contact angle of a water droplet of 10 μl volume on the superhydrophobic surface is $\approx 150°$ ($\pm 4°$). Silica NPs were dispersed in milli-Q water to form suspensions of 5 and 60 wt% weight fraction of NPs ($f_{w,p}$). The average size of nanoparticles, d_p, analyzed from SEM images is 252 nm, while the manufacture data provided is $d_p = 261$ nm, with coefficient of variation of 6.4%.

Three cameras were simultaneously used to capture the side, bottom, and top views of the evaporating droplets. The side view was used to measure the droplet contact angle (θ), base diameter (D), and height (H). Figure 1b provides representative snapshots of an evaporating water droplet laden with 5 wt% nanoparticles on the superhydrophobic substrate. Through top and bottom views, we investigate and analyze the symmetry of the droplet shape, onset of donut formation, and the wetting transition from a partial wetting Cassie-Baxter (CB)[44] to completely wetting Wenzel (W)[52] state.[33,34] The CB wetting state of the drops traps gas underneath between the solid textures, thereby possessing both air-liquid and liquid-solid interfaces. Due to entrapped air, which has a different refractive index from that of water, CB drops reveal bright whereas Wenzel show dark images from the bottom-view camera.[33] Snapshots of evaporating droplets were extracted and analyzed using a Matlab code. All experiments were conducted at room temperature, $25 \pm 1°C$, and relative humidity of $18 \pm 2\%$.

Representative top and bottom views of the final drying assemblies via a simple evaporation in the study are shown in Fig. 1c–f. A low concentration assembly by drying a suspension of 5 wt% NPs resulted in a donut-shaped structure (as revealed by the top-view, Fig. 1c), whereas for a high NP concentration of 60 wt% particles packed and arranged in a spherical structure on the top (Fig. 1e). The bottom views taken when approaching a complete dry (e.g., Fig. 1d and 1f) revealed vivid reflectance color scattered by the photonic structure formed at the bottom of the deposit. The reflectance color changed because of the varying interspace distance between the NPs and effective refractive index during drying, discussed in detail below. The reproducibility of final deposit shape and sequence of reflectance color was checked via conducting independent experiments for at least three times (for each particle concentrations).

Results and Discussion

Figure 2 shows the detailed evaporation dynamics of nanoparticle-laden droplets, namely the time evolution of the droplet base diameter, height, contact angle and shape. The droplet diameter for both concentrations was initially pinned and subsequently receded as the droplets dried out, as shown by the diameter plot in Fig. 2a. In the next stage of evaporation, droplets with 60 wt% of NPs underwent a sudden increase in base diameter (marked by a vertical red arrow). This increase in D is likely caused by the CB to W wetting transition, which occurs at a comparable time, and the formation of the vacuole beneath the droplet. Subsequently, a slight decrease in D was observed until the contact line was pinned once again till a complete dry. On the other hand, low concentration droplets (5 wt%) were pinned after the latter receding regime until the end of the process.

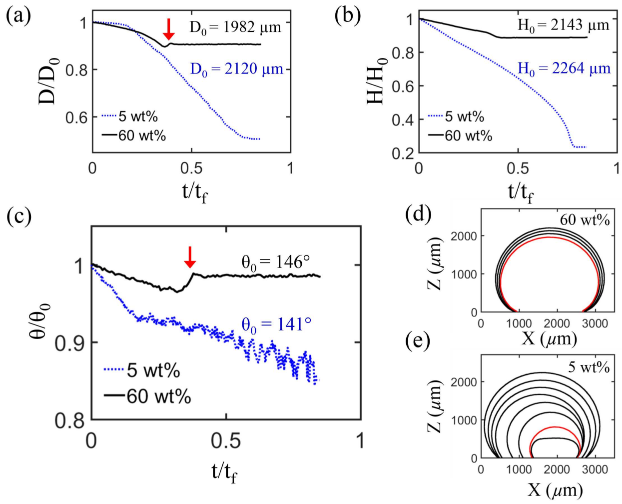

Figure 2: Evolution of normalized base diameter in (a), height in (b), and the tangential contact angle in (c) of evaporating droplets containing $f_{w,p} = 5$ wt% and 60 wt% of nanoparticles on the superhydrophobic surface (measured every 10 s). Here D_0, H_0, and θ_0 are the initial droplet diameter, height, and tangent contact angle (at t=0), respectively. The averaged final evaporation time (t_f) for 5 wt% and 60 wt% experiments are 4668 s and 1485 s, respectively. (d) and (e) Side-view evolutions of evaporating droplets for 60 wt% and 5 wt% of NPs, respectively. Red lines denote the onset of second pinning before complete desiccation.

The droplet height decreased continuously for both concentrations, as revealed in Fig. 2b. The temporal evolution of contact angles is depicted in Fig. 2c. The droplets were initially at Cassie-Baxter state, i.e., $\theta_0 \approx 141°$ and $\approx 146°$ for the 5 wt% and 60 wt% experiments, respectively. They maintained high contact angles ($\gtrsim 120°$) during the entire evaporation process. Similar to the base diameter, 60 wt% droplets underwent a jump in the contact angle. The evolution of the shape of the droplets during evaporation was extracted through image analysis of the side-view snapshots (usually captured at 0.5 fps), as in Fig. 2d and 2e. Red lines highlight the point where the droplets began to pin before complete evaporation.

To further analyze the 60 wt% experiments resulting in quasi-spherical configurations, the deposits were detached from the superhydrophobic substrate and placed upside down in a SEM device. Figure 3a SEM image shows a central cavity (of diameter of $\sim 700\mu$m) formed at the bottom of the dense deposit. The higher magnification SEM images, shown in Fig. 3b-c, reveal the footprints (of depth of $\sim 1-2\mu$m, estimated from Fig. 3c) of micro-pillars in the relatively "flat" region surrounding the central cavity.[35,39,41,53,54] These SEM images suggest that initially the particles-laded drop in the area surrounding the central cavity stayed on top of the pillars, and water did not penetrate completely inside the microstructures (of $h = 14\mu$m) in this area. In other words, the droplet in the flat region stayed at Cassie-Baxter, partial wetting status while air was trapped between the microstructures. However, at a later time of drying, CB to Wenzel wetting transition occurred. As revealed by the bottom-view images of the 60 wt% droplets (e.g., Fig. 1f), water wet the central region of the contact area, where a dome-shaped cavity formed.

Similar observations of central bottom cavity or vacuole have been also reported in a few studies concerning drying of concentrated nanoparticle-laden droplets on superhydrophobic surfaces. Pauchard and Couder,[39] investigated the evaporation of dilute (of volume fraction of particles $f_{v,p} = 15\%$) and concentrated ($f_{v,p} = 40\%$) droplets laden with latex particles resting on a superhydrophobic surface. Consistent with our results, they observed toroidal- and spheroidal-shaped deposits with a cavity underneath for dilute and concentrated droplets, respectively. Accardo et al.[35] studied the evaporation of droplets laden with lysozyme on patterned superhydrophobic surfaces of poly(methyl methacrylate) (PMMA) at room temperature. A hollow sphere was observed from the optical microscopy image of the deposit formed on the substrate. Chen and Evans,[41] explored the desiccation of aqueous droplets laden with alumina nanoparticles on a superhydrophobic surface for different initial concentrations. They observed that in dilute experiments ($f_{v,p} = 5.7\%$) the droplet flattened and left a concave shape on top. In the case of the concentrated droplets ($f_{v,p} = 26\%$), a vacuole was evidenced beneath the deposit. These experimental studies did not focus on the fabrication of 3D photonic crystals but discussed possible mechanism of the formation of bottom cavity of dense drops on SH surfaces.[35,39,41] For instance, due to the high contact angle and small contact area of the drop resting on a SH surface, a region of high humidity may form near the substrate. This may cause a lower evaporative flux in the center and lower part when compared to the upper part of the drop. Hence, water preferentially evaporates in an ascending direction, leading to upward motion of particles, their assembly adjacent to the air-water interface, and a subsequent formation of thick shell. Further drying through this porous but rigid shell formed by the nanoparticles may drive further water flux upwards and consequently result in inward airflow, the growth of air-bubble, and finally leave a dome-shaped cavity below the deposit.[35,39]

It is intriguing and worthy noting that the formation of bottom vacuole was also observed during the evaporation of droplets suspended with different materials (e.g., polymers or proteins) on flat and rough hydrophobic surfaces.[53,54] However, to fully understand and unravel the underlying mechanism of the bottom cavity formation on non-wetting surfaces, particularly for the cases of drying concentrated nanoparticles-laden suspensions on SH surfaces (with a later-time pinned contact line), one would require further work of non-invasive measurements of fluid motion, temperature field, and interior packing dynamics of nanoparticles. These measurements are important for fully utilizing the bottom-up, self-assembly method via evaporation but challenging because of the complexity of the problem involving fluid-particle interactions, internal flow, Marangoni flow, phase change, Cassie-Baxter to Wenzel wetting transition, non-uniform evaporative flux, and contact line movement during the evaporation process on SH surfaces.

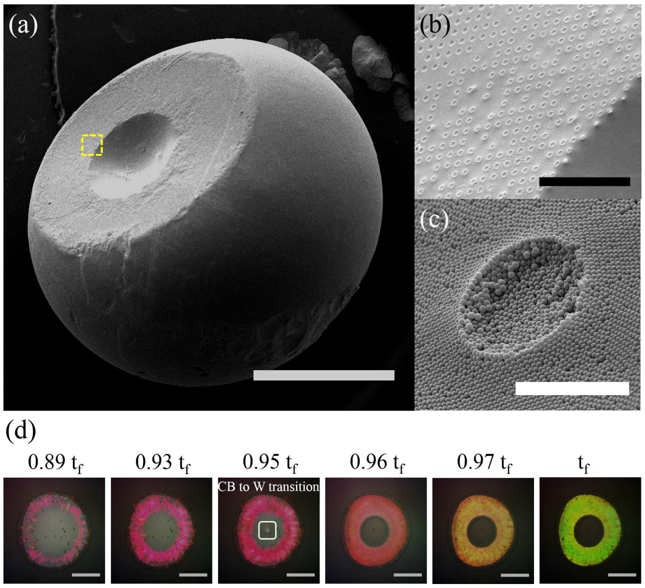

Figure 3: SEM images of the bottom of a dried NP-laden drop (60 ± 5 $wt\%$) with different magnifications: (a) 40×, entire deposit; (b) 600×, footprints of micro-pillars in the flat region shown by dashed area in (a) close to the central bottom cavity; and (c) 10000×, footprint of a single pillar. Scale bars equal to 1000, 100 and 5 μm in (a), (b) and (c), respectively. (d) Optical microscope snapshots (bottom view) of colloidal drop containing 5 wt% of ≈ 252 nm silica NPs at room temperature near the end of evaporation process (i.e., from $0.89 t_f$ to t_f). At $t = 0.95$ t_f the drop undergoes Cassie to Wenzel transition in the case of 5 wt% nanofluid drop. The scale bars in (d) correspond to 500 μm and $t_f = 4770$ s.

To gain more insights into the droplet behavior throughout evaporation, the bottom view images were studied. Figure 3d presents the bottom view snapshots of an evaporating 5wt% droplet in the later stage of evaporation process, i.e., during the second pinning event. The droplet maintained a constant contact area starting from 0.89 t_f (until complete desiccation), transited to Wenzel state at 0.95 t_f in the center of the drop, and eventually dried out. We noticed that droplets with 60 wt% of NPs similarly underwent the wetting transition in the central and bottom region of the drop around a very similar time as D is increased (shown in Fig. 2a). During evaporation, as the silica NPs organize themselves, the overall color of the contact area gradually changes from white to red, orange, yellow and finally green. This color sequence is due to the reflected light scattered by the self-organized NPs, which depends on the drying stage and process (discussed detailed below). Consistently, similar color change from red to green has been recently reported for PhCs created using a microfluidic chip.[55] The capability to guide and control photons can be advantageous for a variety of applications, including protein detection, temperature and humidity control, and various types of sensors.

The SEM images of both top and bottom views of 60 wt% deposits, provided in Fig. 4a, reveal that the particles were organized in a hexagonal pattern. More specifically, from Voronoi analysis over areas of ≈ 11 and ≈ 8 μm^2 for top and bottom views 70% and 76% of NPs have 6 close neighbouring particles, respectively. Hence, most of the particles were packed in a hexagonal pattern. The hexagonal arrangement can be attributed to either a $\{111\}$ plane of a face-centred cubic (FCC) system or a $\{001\}$ plane of a hexagonal closed packed (HCP) system. Despite this, it has been shown through microscopic characterization using SEM images of the packing of nanosized silica spheres[58] in addition to the free energy calculations,[59] that the FCC close packing can be favored over the HCP. In addition, recent investigations using microfluidic emulsions to fabricate supraballs of different sizes (of $O(10-100\mu\text{m})$) shed light on the effects of confinement and drop-size on the ordering and structure of the interior NP-packing.[21,60] For example, micron-sized spherical confinement of emulsion droplets posed on the internal NPs induces frustration regions for crystallization, resulting in disorder and defects in the supraball structures. At high degree of confinement, with a small diameter-ratio of the synthesized supraball (of diameter d_{ball}) to constituent colloids (of diameter d_p), fewer ordered layers exist in the packing structure of the particle assembly.[21] Recent results by both experiments and molecular dynamics simulations showed a structural transition from icosahedral to FCC-ordering arrangement as the number of NPs increased.[60] In other words, the size of the supraparticles, representing the degree of confinement, was found to be a factor controlling the crystalline structure. It was noticed that systems with more than 90,000 particles always resulted in FCC ordering.[60] Applying these results and predictions to our system (where d_p = 261 nm and $d_{ball} \approx 1000$ μm) and considering particle packing fraction of 0.74, there are approximately 4×10^{10} particles in our PhCs, and such low degree of confinement would favor FCC ordering.

The change in the bottom view color during evaporation can be explained based on the combined Bragg-Snell laws[61] for a $\{111\}$ plane of a FCC structure

$$\lambda_{max} = 2d_{\{111\}}n_{eff}, \tag{1}$$

where λ_{max} is the wavelength of the main reflectance peak, $d_{\{111\}}$ is the distance between $\{111\}$ planes and equal to $\sqrt{2/3}D$, with $D = d_p + \epsilon$ being the center-to-center distance between spherical particles of diameter d_p, and surface-to-surface distance of ϵ. For more information see supporting material.[62] Furthermore, n_{eff} is the effective refractive index, which for a medium made of silica particles (p), water (w) and air (a) can be approximated by

$$n_{eff} = \sqrt{f_{v,p}n_p^2 + f_{v,w}n_w^2 + f_{v,a}n_a^2 - sin^2(\alpha)}, \tag{2}$$

where n and f_v correspond to refractive index and volume fraction of each components, respectively. α is the angle of incidence, which is $0°$ for the normal incident.

In addition, the final stage of reflective color scattered by a completely drying of nanofluid droplet on SH surfaces, here we adapt previous model (Eqs. (1)-(2)) and consider the transient, reflection PhC color affected by the varying NP-packing upon drying. During evaporation, the particles tend to organize themselves in a FCC type lattice.[58] The space between particles is initially filled with water having thickness of ϵ on the diagonal (see Fig. S1 in Supplementary Info), as an initial stage (1), and subsequently both air and water occupy the space as evaporation goes on, in stage (2). In other words, stage (1) modelled corresponds to the range where the particle volume fraction varies from the melting volume fraction ($f_{v,p}$ = 0.545) to the random close packing limit, where $f_{v,p}$ = 0.64. Based on the phase diagrams of drying colloids containing hard spheres, a homogeneous crystal phase would emerge around the melt-

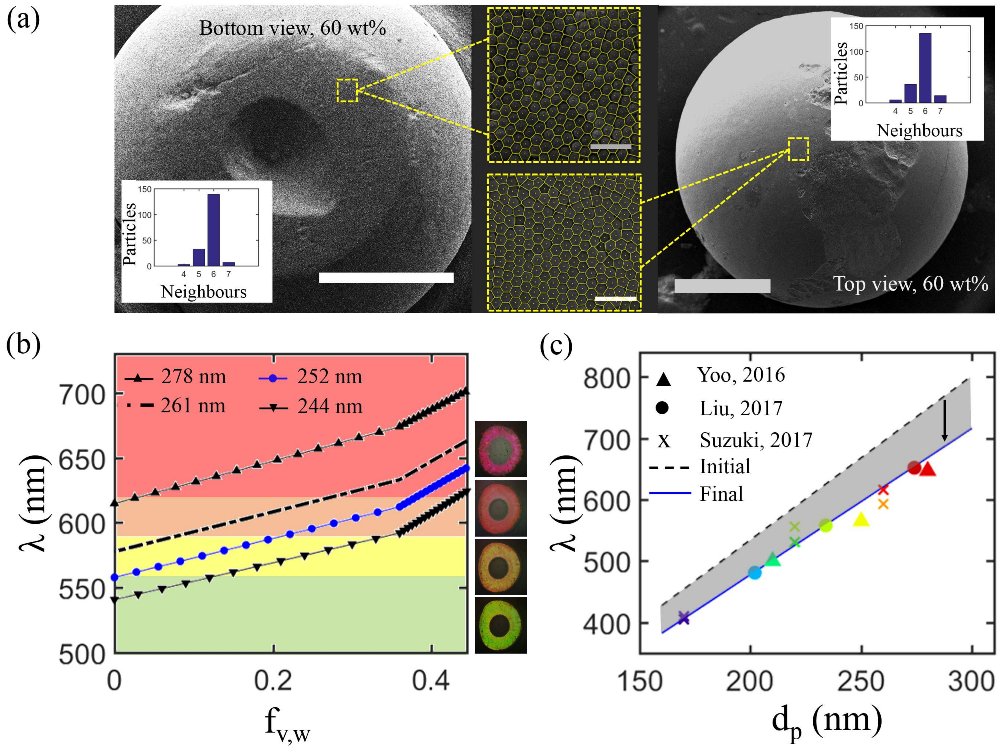

Figure 4: (a) Top and bottom view SEM image of self-assembled silica particles, forming a top-spherical deposit with a cavity underneath on superhydrophobic surface after evaporation. Yellow dashed squares depict the Voronoi analysis of the packing of nanoparticles based on the image acquired from high magnification SEM. Bar diagrams reveal the number of close neighbors each particles have in the region under study (dashed square). Zoomed out scale bars equal 800 μm; Scale bars in insets equal 1 μm. (b) Analysis of the reflected colors from the bottom view of an evaporating droplet using Bragg-Snell equation: $\lambda = 2\sqrt{2/3} \cdot (d_p + \epsilon) \cdot n_{eff}(f_v)$, where d_p is the particle size, ϵ is the water layer thickness around particles, and $n_{eff}(f_v)$ is the effective refractive index as a function of the volume fractions (f_v) of particles (p), water (w), and air (a). (c) Prediction by our current model on the reflected wavelengths compared with existing experimental data[9,56,57] (obtained from the bottom-view of a desiccating polystyrene colloidal droplet). The solid-line is predicted for complete evaporation, considering no water layer around particles, meaning $\epsilon = 0$, while the dashed-line corresponds to the case where there is water around particles.

ing volume fraction and, hence, one can expect a reflected color scattered by the homogeneous structure.[63,64] It is assumed that there are only water and silica particles inside the system at the stage (1), i.e., $f_{v,a} = 0$. During the stage (2), as the volume fraction of water diminishes due to evaporation, both the volume fractions of particles ($f_{v,p}$) and air ($f_{v,a}$) increase, while $f_{v,p}$ is assumed to increase from the random close packing limit. This stage is completed once the maximum cubic close packing limit, where $f_{v,p} = 0.74$, is reached. See Supplementary Material for the detailed analysis.[62]

The results of the optimal reflected color based on this model are presented in Fig. 4b. Based on the coefficient of variation provided by the manufacturing company (6.4%), the reflectance peaks were calculated for three particle sizes, namely, 244 nm, 261 nm (mean diameter) and 278 nm. The reflectance peaks were also evaluated for the average particle size (252 nm), analyzed using SEM images of self-assembly nanoparticles, such as the insert in Fig. 4a. As revealed in Fig. 4b, larger particles result in reflection of longer wavelengths. More specifically, for nanoparticles of d_p =278 nm, the wavelength varied from red to orange. For 261 nm particles, the color shifted from red to yellow, while 244 nm NPs covered the orange to green wavelength region. In this analysis, the reflectance peaks varied from red to green for average particle size of 252 nm, which agree well with our experimental data shown in Fig. 3d. This simplified model would capture the overall trend of the reflectance light scattered globally. However, during drying dewetting process can happen locally[65] and thus change the local n_{eff} slightly. Consequently, there may be slight color deviation from the overall reflectance color observed or predicted, especially at the edges of deposits where surface curvature presents, as revealed in Fig. 3d.

We further extended our analysis to drying colloidal suspensions for different sizes and materials found from the literature. In Fig. 4c, we predicted the sequential variation of the reflected wavelength from the bottom view during evaporation (grey area) for polystyrene particles ($n_p = 1.59$) of varying diameters (170 to 340 nm) used in previous studies.[9,56,57] The top dashed line corresponds to the reflected wavelength at the beginning of stage (1), while the lower solid line is the wavelength reflected at the end of stage (2), when the deposit was completely dried out. The linear relationship between the particle size and the reflected wavelength from the deposit has been evidenced by recent experiments.[66,67] The vertical downward arrow depicts the variation in the wavelength of a typical droplet during desiccation. Moreover, our analyses show good agreement with existing experimental work.[9,56,57] The different symbol colors represent the final reflectance wavelength obtained by the corresponding materials.

Conclusions

We have successfully fabricated photonic crystals of different sizes and shapes using evaporation-driven self-assembly of nanoparticles on a superhydrophobic surface. Toroidal and spherical shaped crystals have been created by aqueous droplets suspended with 5 wt% and to 60 wt% of NPs, respectively. The high-resolution snapshots captured from simultaneous top, bottom, and side views show distinct evaporating processes for different nanoparticle concentrations. The nanofluid droplets with 60 wt% nanoparticles maintained a large contact angle with a pinned contact line from the early drying stage, but a decreasing contact angle, droplet diameter, and height for droplets laden with 5 wt% nanoparticles. In addition, scanning electron microscopy images of the crystal structures proved that particles organized themselves into hexagonal patterns. From the bottom view evolution of the droplets, a change in overall color from red to green was observed for both NP concentrations. A model considering the particle diameter, material, interplanar distance, and the particle-water-air content of the droplet was developed to predict the color sequence during evaporation. The predictions agree well with our data for silica NPs and other experimental results with polystyrene NPs. The model can be further utilized effectively to predict the reflected light/color by photonic crystals fabricated and self-assembled via simple evaporation.

Acknowledgement MBB and PAT acknowledges funding from Natural Sciences and Engineering Research Council of Canada (NSERC) and Alberta Innovate (AI). PAT holds a Canada Research Chair in Fluids and Interfaces.

Supporting Information Available: Supplemental Material contains (i) the details of the model and (ii) additional SEM images for Voronoi analyses. This material is available free of charge via the Internet at `http://pubs.acs.org/`.

References

(1) Zhang, Z.; Zhu, W. Controllable fabrication of a flexible transparent metallic grid conductor based on the coffee ring effect. J. Mater. Chem. C **2014**, 2, 9587–9591.

(2) Aoki, K.; Guimard, D.; Nishioka, M.; Nomura, M.; Iwamoto, S.; Arakawa, Y. Coupling of quantum-dot light emission with a three-dimensional photonic-crystal

nanocavity. Nat. Photonics **2008**, 2, 688–692.

(3) Bigdeli, M. B.; Fasano, M. Thermal transmittance in graphene based networks for polymer matrix composites. Int. J. Therm. Sci. **2017**, 117, 98–105.

(4) Bigdeli, M. B.; Fasano, M.; Cardellini, A.; Chiavazzo, E.; Asinari, P. A review on the heat and mass transfer phenomena in nanofluid coolants with special focus on automotive applications. Renewable Sustainable Energy Rev. **2016**, 60, 1615–1633.

(5) Syed, A.; Mangano, L.; Mao, P.; Han, J.; Song, Y.-A. Creating sub-50 nm nanofluidic junctions in a PDMS microchip via self-assembly process of colloidal silica beads for electrokinetic concentration of biomolecules. Lab. Chip. **2014**, 14, 4455–4460.

(6) Shen, W.; Li, M.; Ye, C.; Jiang, L.; Song, Y. Direct-writing colloidal photonic crystal microfluidic chips by inkjet printing for label-free protein detection. Lab-on-a-chip **2012**, 12, 3089–3095.

(7) Jelle, A. A.; Ghuman, K. K.; O'Brien, P. G.; Hmadeh, M.; Sandhel, A.; Perovic, D. D.; Singh, C. V.; Mims, C. A.; Ozin, G. A. Highly efficient ambient temperature CO2 photomethanation catalyzed by nanostructured RuO2 on silicon photonic crystal support. Adv. Energy Mater. **2018**, 8, 1702277.

(8) Huang, C.; Cheng, Y.; Zhang, H.; Wei, J. Janus multicolored photonic crystal beads for real-time magnetic responsive patterns. Part. Part. Syst. Charact. **2019**, 36, 1900238.

(9) Yoo, J.-H.; Kwon, H.-J.; Paeng, D.; Yeo, J.; Elhadj, S.; Grigoropoulos, C. P. Facile fabrication of a superhydrophobic cage by laser direct writing for site-specific colloidal self-assembled photonic crystal. Nanotechnology **2016**, 27, 145604.

(10) Ozin, G. A.; Hou, K.; Lotsch, B. V.; Cademartiri, L.; Puzzo, D. P.; Scotognella, F.; Ghadimi, A.; Thomson, J. Nanofabrication by self-assembly. Mater. Today **2009**, 12, 12–23.

(11) Schaffner, M.; England, G.; Kolle, M.; Aizenberg, J.; Vogel, N. Combining bottom-Up self-assembly with top-down microfabrication to create hierarchical inverse opals with high structural order. Small **2015**, 11, 4334–4340.

(12) Goerlitzer, E. S.; Klupp Taylor, R. N.; Vogel, N. Bioinspired photonic pigments from colloidal self-assembly. Adv. Mater. **2018**, 30, 1706654.

(13) Lee, W.; Chan, A.; Bevan, M. A.; Lewis, J. A.; Braun, P. V. Nanoparticle-mediated epitaxial assembly of colloidal crystals on patterned substrates. Langmuir **2004**, 20, 5262–5270.

(14) Demirörs, A. F.; Johnson, P. M.; van Kats, C. M.; van Blaaderen, A.; Imhof, A. Directed self-assembly of colloidal dumbbells with an electric field. Langmuir **2010**, 26, 14466–14471.

(15) Ding, T.; Song, K.; Clays, K.; Tung, C.-H. Fabrication of 3D photonic crystals of ellipsoids: convective self-assembly in magnetic field. Adv. Mater. **2009**, 21, 1936–1940.

(16) Kawamura, A.; Kohri, M.; Morimoto, G.; Nannichi, Y.; Taniguchi, T.; Kishikawa, K. Full-color biomimetic photonic materials with iridescent and non-iridescent structural colors. Sci. Rep. **2016**, 6, 33984.

(17) Zheng, H.; Ravaine, S. Bottom-up assembly and applications of photonic materials. Crystals **2016**, 6, 54.

(18) Miglani, A.; Basu, S. Sphere to ring morphological transformation in drying nanofluid droplets in a contact-free environment. Soft Matter **2015**, 11, 2268–2278.

(19) Wang, J.; Wang, L.; Song, Y.; Jiang, L. Patterned photonic crystals fabricated by inkjet printing. J. Mater. Chem. C **2013**, 1, 6048–6058.

(20) Zhang, M.-Y.; Xu, K.; Xu, J.-H.; Luo, G.-S. Self-assembly kinetics of colloidal particles inside monodispersed micro-Droplet and fabrication of anisotropic photonic crystal micro-particles. Crystals **2016**, 6, 122.

(21) Vogel, N.; Utech, S.; England, G. T.; Shirman, T.; Phillips, K. R.; Koay, N.; Burgess, I. B.; Kolle, M.; Weitz, D. A.; Aizenberg, J. Color from hierarchy: diverse optical properties of micron-sized spherical colloidal assemblies. Proc. Natl. Acad. Sci. U.S.A. **2015**, 112, 10845–10850.

(22) Lafuma, A.; Quéré, D. Superhydrophobic states. Nat. Mater. **2003**, 2, 457.

(23) Quéré, D. Wetting and roughness. Annu. Rev. Mater. Res. **2008**, 38, 71–99.

(24) Celia, E.; Darmanin, T.; de Givenchy, E. T.; Amigoni, S.; Guittard, F. Recent advances in designing superhydrophobic surfaces. J. Colloid Interface Sci. **2013**, 402, 1–18.

(25) Park, J.; Lim, H.; Kim, W.; Ko, J. S. Design and fabrication of a superhydrophobic glass surface with micro-network of nanopillars. J. Colloid Interface Sci. **2011**, 360, 272–279.

(26) Erbil, H. Y. Evaporation of pure liquid sessile and spherical suspended drops: A review. Adv. Colloid Interface Sci. **2012**, 170, 67–86.

(27) Reyssat, M.; Yeomans, J.; Quéré, D. Impalement of fakir drops. EPL **2007**, 81, 26006.

(28) Bico, J.; Thiele, U.; Quéré, D. Wetting of textured surfaces. Colloids Surf., A **2002**, 206, 41–46.

(29) Callies, M.; Quéré, D. On water repellency. Soft matter **2005**, 1, 55–61.

(30) Moulinet, S.; Bartolo, D. Life and death of a fakir droplet: Impalement transitions on superhydrophobic surfaces. Eur. Phys. J. E: Soft Matter Biol. Phys. **2007**, 24, 251–260.

(31) Jung, Y.; Bhushan, B. Wetting behaviour during evaporation and condensation of water microdroplets on superhydrophobic patterned surfaces. J. Microsc. **2008**, 229, 127–140.

(32) Murakami, D.; Jinnai, H.; Takahara, A. Wetting transition from the Cassie–Baxter state to the Wenzel state on textured polymer surfaces. Langmuir **2014**, 30, 2061–2067.

(33) Tsai, P.; Lammertink, R.; Wessling, M.; Lohse, D. Evaporation-triggered wetting transition for water droplets upon hydrophobic microstructures. Phys. Rev. Lett. **2010**, 104, 116102.

(34) Bussonniére, A.; Bigdeli, M. B.; Chueh, D.-Y.; Liu, Q.; Chen, P.; Tsai, P. A. Universal wetting transition of an evaporating water droplet on hydrophobic micro-and nano-structures. Soft matter **2017**, 13, 978–984.

(35) Accardo, A.; Gentile, F.; Mecarini, F.; De Angelis, F.; Burghammer, M.; Di Fabrizio, E.; Riekel, C. In situ X-ray scattering studies of protein solution droplets drying on micro-and nanopatterned superhydrophobic PMMA surfaces. Langmuir **2010**, 26, 15057–15064.

(36) Marín, Á. G.; Gelderblom, H.; Susarrey-Arce, A.; van Houselt, A.; Lefferts, L.; Gardeniers, J. G.; Lohse, D.; Snoeijer, J. H. Building microscopic soccer balls with evaporating colloidal fakir drops. Proc. Natl. Acad. Sci. U.S.A. **2012**, 109, 16455–16458.

(37) Brunet, P. Particle deposition after droplet evaporation on ultra-hydrophobic micro-textured surfaces. Soft Matter **2012**, 8, 11294–11301.

(38) Accardo, A.; Di Stasio, F.; Burghammer, M.; Riekel, C.; Krahne, R. Nanocrystal self-assembly into hollow dome-shaped microstructures by slow solvent evaporation on superhydrophobic substrates. Part. Part. Syst. Charact. **2015**, 32, 524–528.

(39) Pauchard, L.; Couder, Y. Invagination during the collapse of an inhomogeneous spheroidal shell. EPL **2004**, 66, 667.

(40) Rastogi, V.; Melle, S.; Calderon, O. G.; Garcia, A. A.; Marquez, M.; Velev, O. D. Synthesis of light-diffracting assemblies from microspheres and nanoparticles in Droplets on a Superhydrophobic Surface. Adv. Mater. **2008**, 20, 4263–4268.

(41) Chen, L.; Evans, J. R. Drying of colloidal droplets on superhydrophobic surfaces. J. Colloid Interface Sci. **2010**, 351, 283–287.

(42) Sperling, M.; Gradzielski, M. Droplets,

evaporation and a superhydrophobic surface: Simple tools for guiding colloidal particles into complex materials. Gels **2017**, 3, 15.

(43) Sperling, M.; Spiering, V. J.; Velev, O. D.; Gradzielski, M. Controlled formation of patchy anisometric fumed silica supraparticles in droplets on bent superhydrophobic surfaces. Part. Part. Syst. Charact. **2017**, 34, 1600176.

(44) Cassie, A.; Baxter, S. Wettability of porous surfaces. Trans. Faraday Soc. **1944**, 40, 546–551.

(45) Wooh, S.; Huesmann, H.; Tahir, M. N.; Paven, M.; Wichmann, K.; Vollmer, D.; Tremel, W.; Papadopoulos, P.; Butt, H.-J. Synthesis of mesoporous supraparticles on superamphiphobic surfaces. Adv. Mater. **2015**, 27, 7338–7343.

(46) Sekido, T.; Wooh, S.; Fuchs, R.; Kappl, M.; Nakamura, Y.; Butt, H.-J.; Fujii, S. Controlling the structure of supraballs by pH-Responsive particle assembly. Langmuir **2017**, 33, 1995–2002.

(47) Vogelaar, L.; Barsema, J. N.; van Rijn, C. J.; Nijdam, W.; Wessling, M. Phase separation micromolding – PSμM. Adv. Mater. **2003**, 15, 1385–1389.

(48) Vogelaar, L.; Lammertink, R. G.; Barsema, J. N.; Nijdam, W.; Bolhuis-Versteeg, L. A.; Van Rijn, C. J.; Wessling, M. Phase separation micromolding: a new generic approach for microstructuring various materials. Small **2005**, 1, 645–655.

(49) Tsai, P.; Peters, A. M.; Pirat, C.; Wessling, M.; Lammertink, R. G.; Lohse, D. Quantifying effective slip length over micropatterned hydrophobic surfaces. Phys. Fluids **2009**, 21, 112002.

(50) Tsai, P.; Pacheco, S.; Pirat, C.; Lefferts, L.; Lohse, D. Drop impact upon micro-and nanostructured superhydrophobic surfaces. Langmuir **2009**, 25, 12293–12298.

(51) Tsai, P.; Hendrix, M. H.; Dijkstra, R. R.; Shui, L.; Lohse, D. Microscopic structure influencing macroscopic splash at high Weber number. Soft Matter **2011**, 7, 11325–11333.

(52) Wenzel, R. N. Resistance of solid surfaces to wetting by water. Ind. Eng. Chem. **1936**, 28, 988–994.

(53) Manukyan, S.; Sauer, H. M.; Roisman, I. V.; Baldwin, K. A.; Fairhurst, D. J.; Liang, H.; Venzmer, J.; Tropea, C. Imaging internal flows in a drying sessile polymer dispersion drop using Spectral Radar Optical Coherence Tomography (SR-OCT). J. Colloid Interface Sci. **2013**, 395, 287–293.

(54) Sadek, C.; Tabuteau, H.; Schuck, P.; Fallourd, Y.; Pradeau, N.; Le Floch-Fouéré, C.; Jeantet, R. Shape, shell, and vacuole formation during the drying of a single concentrated whey protein droplet. Langmuir **2013**, 29, 15606–15613.

(55) Wang, H.; Liu, Y.; Chen, Z.; Sun, L.; Zhao, Y. Anisotropic structural color particles from colloidal phase separation. Sci. Adv. **2020**, 6, eaay1438.

(56) Suzuki, N.; Iwase, E.; Onoe, H. Microfluidically patterned dome-shaped photonic colloidal crystals exhibiting structural colors with low angle dependency. Adv. Opt. Mater. **2017**, 5, 1600900.

(57) Liu, F.; Xiu, J.; Tang, B.; Zhao, D.; Zhang, S. Dynamic monitoring of thermally assisted assembly of colloidal crystals. J. Mater. Sci. **2017**, 52, 7883–7892.

(58) Mıguez, H.; Lopez, C.; Meseguer, F.; Blanco, A.; Vazquez, L.; Mayoral, R.; Ocana, M.; Fornes, V.; Mifsud, A. Photonic crystal properties of packed submicrometric SiO_2 spheres. Appl. Phys. Lett. **1997**, 71, 1148–1150.

(59) Woodcock, L. Entropy difference between the face-centred cubic and hexagonal close-packed crystal structures. Nature **1997**, 385, 141.

(60) De Nijs, B.; Dussi, S.; Smallenburg, F.; Meeldijk, J. D.; Groenendijk, D. J.; Filion, L.; Imhof, A.; Van Blaaderen, A.; Dijkstra, M. Entropy-driven formation of large icosahedral colloidal clusters by spherical confinement. Nat. Mater. **2015**, 14, 56.

(61) Ozin, G. A.; Arsenault, A. C.; Cade-

martiri, L. Nanochemistry: a chemical approach to nanomaterials; RSC, 2009.

(62) See Supplemental Material at [URL will be inserted by publisher] for (i) details of the model and (ii) additional SEM images for Voronoi analyses.

(63) Pusey, P.; van Megen, W. Phase behaviour of concentrated suspensions of nearly hard colloidal spheres. Nature **1986**, 320, 340–342.

(64) Yamanaka, O. T., J; Toyotama, A. Colloidal Crystals, Pattern Formations and Oscillatory Phenomena; Elsevier, 2013; pp 165–198.

(65) Burgess, I. B.; Abedzadeh, N.; Kay, T. M.; Shneidman, A. V.; Cranshaw, D. J.; Lončar, M.; Aizenberg, J. Tuning and freezing disorder in photonic crystals using percolation lithography. Sci. Rep. **2016**, 6, 19542.

(66) Zhu, Z.; Liu, J.-D.; Liu, C.; Wu, X.; Li, Q.; Chen, S.; Zhao, X.; Weitz, D. A. Microfluidics-assisted assembly of injectable photonic hydrogels toward Reflective Cooling. Small **2020**, 16, 1903939.

(67) Guo, R.; Wang, D.-N.; Wei, Y.-Y.; Zhang, Y.-Z.; Yang, C.-G.; Xu, Z.-R. Colloidal photonic crystal array chip based on nanoparticle self-assembly on patterned hydrophobic surface for signal-enhanced fluorescent assay of adenosine. Microchim. Acta **2020**, 187, 1–10.

Graphical TOC Entry